Experimental Cross Sections for Electron Excitation of the 2s ^{2}S $\rightarrow$ 2p ^{2}P Transition in C^{3+}

J. B. Greenwood, Steven J. Smith, and A. Chutjian

Jet Propulsion Laboratory, California Institute of Technology, Pasadena, CA 91109

E. Pollack

Physics Department, University of Connecticut, Storrs, CT 06269-3046

Abstract

Experimental cross sections are reported for electron-excitation of the allowed 2s ^{2}S $\rightarrow$ 2p ^{2}P transition in C^{3+}. Center-of-mass energies are from below threshold (7.00 eV), through threshold (8.00 eV), and up to approximately 1.5 × threshold (12 eV). Present results are found to overlap earlier energy-loss data reported to energies of 8.45 eV. The data are also compared with other optical-emission results for this dipole-allowed transition, and with several theoretical calculations. A novel "electronic aperture" is described which allows discrimination against elastically-scattered electrons, with their larger Larmor radii, in experiments with magnetically-confined ions or electrons.

multiply-charged ions

I. INTRODUCTION

Electron-impact excitation of the allowed $2s\,{}^2S \rightarrow 2p\,{}^2P$ transition in C^{3+} is a process which is observed frequently in solar [1], stellar [2], the interstellar medium [3], and laboratory fusion plasmas [4,5]. In both the astronomical and fusion environments the $2s \rightarrow 2p$ transition serves as a useful diagnostic of electron temperature, emitted power, and opacity. Almost all available results on cross sections or collisions strengths in multiply-charged ions (MCIs) are theoretical. Measurements involving MCIs are therefore needed to provide "ground truth" for the calculations. Those theories which provide good agreement with experiment can then be used to calculate cross sections for transitions which have not, or cannot (the lines are too dense) be measured. We present herein new measurements of absolute electron excitation cross sections for the $2s \rightarrow 2p$ transition in C^{3+}. These measurements overlap, near threshold, earlier results using the electron energy-loss method [6], and at higher energies several optical-emission measurements on the unresolved resonance doublet $2s\,{}^2S_{1/2} \rightarrow 2p\,{}^2P_{1/2,\,3/2}$ at 154.8 and 155.1 nm [7-9]. A summary of the experimental facility and the energy-loss method is given in *Sec. II.A*. Recent modifications to the instrument control and data-acquisition system are explained in *Sec. II.B*. An "electronic aperture" (EA) is used to filter elastically-scattered electrons from the energy-loss spectrum, and is described in *Sec. II.C*. Present results and discussion of all data are presented in *Sec. III*.

II. EXPERIMENTAL

A. The energy-loss method

Absolute excitation cross sections for both threshold and above-threshold excitation of the $2s \rightarrow 2p$ optically-allowed (dipole) transition in C^{3+} were measured using the newly-installed 14.0

GHz electron-cyclotron resonance ion source (*Caprice*) at JPL [10-12]. This source is presently connected to three separate MCI beam lines dedicated to measurements of excitation cross-sections, lifetimes of metastable MCI states, and MCI-neutral charge-exchange/X-ray emission cross sections [12,13]. A schematic diagram of the *Caprice* source and beam lines is shown in Fig. 1.

The basic experimental approach in the e - C^{3+} work was the same as in previous work on e - S^+ scattering [14], and only differences are noted here. The equation relating the experimentally-measured parameters to $\sigma(E)$, the final excitation cross section in cm^2, is given by

$$\sigma(E) = \frac{\Re q e^2 \mathscr{F}}{\epsilon I_i I_e L} \left| \frac{\upsilon_e \upsilon_i}{\upsilon_e - \upsilon_i} \right| , \qquad (1)$$

where $\Re$ is the total signal rate (s^{-1}), q is the ion charge, e is the electron charge, I_e and I_i are the electron and ion currents, respectively, υ_e and υ_i are the electron and ion velocities ($cm\ s^{-1}$), respectively, L is the merged path length (cm), ϵ is the efficiency of the rejection grids-microchannel plate detection system (dimensionless), $\mathscr{F}$ is the overlap factor between the electron and ion beams (cm^2).

B. Modifications to the data acquisition system

The data acquisition system used in our previous work was significantly upgraded to allow total computer (PC) control of the beams modulation, position-sensitive detector (PSD) transfers, stepper-motor control for measuring beams profiles with the moving vanes, and reading/storing of transmitted electron and ion currents through the vanes. A schematic diagram of the present control

system is given in Fig. 2. Control was through two digital I/O boards: one to generate beams chopping voltages and channel gating pulses, and a second to accept the PSD's (x, y) position and STROBE rates, together with the correlated beams chopping channel. A PC output signal was input to high-voltage pulsing circuitry [15] used to generate moderately fast (100 ns risetime), high-voltage (100-400 V) modulation pulses to the ion and electron deflection plates. A third counter-timer board accepted the PSD RATE signal, correlated with the chopping channel. Separation of the channels, corresponding to the different beams chopping phases (ABCD, see Fig. 2), was important as each channel has a different counting rate, hence incurs a different deadtime correction. The counter-timer board also controlled the stepper motor and received digitized, transmitted electron and ion beams currents from the vanes' Faraday cups.

C. The Electronic Aperture

Elastic electron scattering from the MCIs can be an unwelcome addition to the electron-ion inelastic scattering signal [13,16]. It has been noted earlier that the trochoidal analyzing plates can only separate electrons of differing axial velocities [17]. Hence, two electrons having the same axial velocity (a low-angle inelastically-scattered electron with a high-angle elastically-scattered electron) will strike the same position on the PSD, leading to an "aliasing" of signal . The elastic scattering differential cross section increases approximately as q^2 of the MCI. Even for the case of e - C^{3+} scattering, this corresponds to a factor of about nine increase in elastic effects relative to a singly-charged target. Hence it is essential to filter out the elastic component as completely as possible.

When an electron of longitudinal velocity υ_e and mass m_e is scattered at laboratory (LAB) angle ϑ from an ion, the electron will spiral in the uniform magnetic field B along a trajectory of

4

diameter d given by $d = 2m_e\, v_e \sin\vartheta\, /\, eB$, with the center of the spiral displaced from its starting position by the distance $d/2$. Since electrons elastically-scattered through a laboratory (LAB) angle ϑ will in general have larger transverse velocities compared to inelastically-scattered electrons at that ϑ, they will have larger spiral diameters. This difference can be used to remove these electrons, while transmitting the desired inelastically-scattered ones. In experiments by Bell, *et al.* [16] a series of fixed, physical apertures was used to remove the elastically-scattered electrons. With apertures of diameter D centered on the beam axis, electrons with scattering angles greater than some ϑ_{max} will hit the physical edge of the aperture and be removed. Here the value of D is given by

$D = 4m_e\, v_e \sin\vartheta_{max}\, /eB.$

It is highly desirable to have an adjustable ϑ_{max} for a given scattered electron energy. It should be as small as possible to block the elastic electrons and yet transmit all inelastic electrons. The only way to do this with fixed, physical apertures is to vary B. However, as the whole interaction region is immersed in this field, all aspects of the primary and scattered electron beams will be affected. A more favorable approach is to change D itself. Setting up a series of mechanically-adjustable apertures, externally controlled in an ultrahigh vacuum system would add complexity to an already difficult experiment. As an alternative, we have developed an "electronic aperture" (EA) which uses externally-adjustable electrostatic potentials, on an array of poles, to alter the effective cutoff diameter D. This array consists of 16 poles with centers on a 15-mm dia circle about the beam axis. Each pole is 2.00 mm dia, 25 mm long, and made of CP-grade titanium. A cross section through the aperture, including equipotentials, is shown in Fig. 3. The pole array is surrounded by a cylindrical shield. In addition, grounded entrance and exit apertures, each of 11 mm dia, are provided. Equal and opposite potentials are placed on adjacent poles. As a result there is a net

cancellation of both the electric potential and electric field at the center of the array. Electrons traveling "sufficiently close" to the array axis are therefore undeflected. Electrons having larger Larmor radii (elastic electrons with relatively large velocities perpendicular to the magnetic field direction) will make excursions closer to one of the poles, and their trajectories will be dramatically affected. These electrons spiral into the rods, or into the surrounding shield.

To quantify these effects we have calculated the electric field and resulting electron trajectories using the SIMION 3D fields-and-trajectories software code [18]. The calculated electric field as a function of radial distance from the central axis of the EA, with various potentials placed on the rods, is shown in Fig. 4 . As expected, the field rises steeply as one approaches the rods. Samples of several SIMION- calculated trajectories of electrons injected into the EA are shown in Fig. 5. Since there is negligible field at the center, electrons with small spiral diameters can pass through unaffected (Fig. 5, upper), while electrons with larger energies and at larger distances from the central axis will suffer strong deviations in their trajectories. These are ejected into the rods or shield (Fig. 5, lower). The spatial extent of the central zero-field region can be adjusted. Qualitatively, if an electron approaches one of the *negative* poles it slows down. This produces a tighter spiral, and a kink in the trajectory. When the electron orbit re-enters the null-field region its spiral center has been displaced. If this displacement is sufficiently large the electron will be channeled out when it approaches an adjacent positive electrode. When an electron approaches a *positive* pole, its Larmor radius will become expanded, and it will hit either the pole or shield.

In order to understand the transmission properties of the array SIMION was used to launch a series of approximately 2000 trajectories at each of four values of magnetic field, using starting energies and (polar θ, azimuthal ϕ) angles in the center-of-mass (CM) frame. Starting positions were randomized within a 0.5 mm diameter cylinder to simulate the merged electron beam diameter;

starting azimuthal angles were also randomized in the interval $(0, 2\pi)$. Starting CM energies were randomized within the range 2-20 eV for the polar angles of interest and for different magnetic field strengths. The fraction of starting trajectories passed by the aperture was obtained for different multipole potentials, as a function of starting spiral diameter d. Results of transmission are given in Fig. 6 at $B = 2.5$ and 5.0 mT. One clearly sees the cutoff curves moving towards smaller d (effective aperture size decreasing) as one increases the magnitude of the poles potential: the spatial extent of the central null-field becomes smaller. Also, as one increases B, the diameter of the spirals becomes smaller, and hence a higher electrode potential is needed to eject electrons with the smaller d. It is found in general that the effective aperture diameter depends only upon d and B. In the present geometry the aperture diameter, as calculated, could be varied in the range 7-12 mm (corresponding to the 10% transmission points).

III. Experimental results

The methods for data acquisition and data analysis in e - C^{3+} scattering were similar to those used in Ref. [14]. Care had to be taken to tune the electron and ion beams through the center of the EA, while maintaining good spatial overlap over the 20 cm merged length (as measured with the four rotating vanes), and minimum backgrounds from each beam. Ion and electron beam currents were typically in the range 3-30 nA, and 20-70 nA, respectively. The ion beam was the dominant source of background, with a maximum rate of about 1 kHz/nA. No metastable levels in the primary C^{3+} beam are expected for this Li-like ion. Nevertheless we used the beam-attenuation method [14] as a further check to see that the beam was exclusively in the ground-state. Within the statistical accuracy of the measurements, the fraction of metastables was found to be less than 5%.

Extensive trajectory calculations were performed at the energies of the data set, for elastic and inelastic electrons. Operationally, the voltages on the positive and negative poles were increased to the level where transmission of the inelastically-scattered electrons would be impeded. These pole voltages result in rejection of most of the large-angle elastic scattering events (depending on the CM energy above threshold). Near threshold the EA works well, and no elastic electrons are detected. While elastically-scattered electrons are transmitted through the EA, they are well-separated on the PSD due to their large longitudinal velocity and hence small drift in the AP. Illustrative trajectories are shown in Fig. 7 for three cases corresponding to an incident CM energy of 9 eV. In Fig. 7(a) and (b) one has trajectories for elastically-scattered electrons, with the EA voltages turned on and off, respectively. In Fig. 7(a) almost all the trajectories have been eliminated (within the EA: see trajectories terminating on the poles) due to the filtering. The few remaining transmitted trajectories, corresponding to low-angle elastic electrons, do not have sufficient deflection to reach the PSD. Trajectories of the inelastically-scattered electrons, with 1 eV residual energy, are shown in Fig. 7 (c) at the same EA voltage setting as in Fig. 7(a). There is no loss of electrons either in the EA or on the PSD. Naturally there are cases further above threshold where the energy-angle separations will result in some overlap of the elastic and inelastic electrons.

A subtler rejection effect arises from further displacement due to a broader and tilted beam-shear pattern [19] for the elastic electrons relative to the inelastic electrons. This arises because large-angle elastic electrons, traveling with larger Larmor radii than the inelastic electrons, experience a greater excursion in electric potential within AP as they execute their orbital loops. Finally, high- and low-voltage discrimination grids in front of the PSD are used to subtract out contributions from higher-energy electrons, or possibly soft x-rays reflected from metal surfaces.

The general pattern emerges that the small number of large-angle, elastically-scattered

electrons transmitted by the EA are effectively dispersed at the PSD. An even smaller number that overlap the region of interest (ROI) on the PSD are accounted for by the incremental subtraction method [17]. At each CM energy the (x,y) signal at the PSD, consisting of all the inelastic and a small fraction of elastic electrons) is analyzed using the 3D trajectories code. The fractional contribution of the elastic signal to the cross section $\sigma(E)$ is calculated by multiplying the number of calculated "hits" for a given ϑ by the theoretical DCS at the CM angle θ corresponding to LAB angle ϑ. This DCS is taken from accurate calculations of elastic-scattering phase shifts [20]. Thus, this method completes four levels of defense against elastically-scattered electrons: trochoidal dispersion, electronic aperture, discrimination grids, and differential beam shear.

Present experimental results are given in Fig. 8, and tabulated in Table 1. Errors are given at the 1.7σ or 90% confidence level, and total error bars are shown for each data point (rather than relative errors with isolated total error bars). Details of the individual uncertainties may be found in Table I of Ref. [21]. The energy spread in the present data is 250 meV (FWHM). Earlier excitation data are also shown in Fig. 8. These include electron energy-loss measurements near threshold [6] taken with a stated electron energy spread of 170 meV, and optical-emission results [7-9] taken with broader spreads of 1.7 [9] and 2.3 eV [7,8]. From the experimental comparisons in Fig. 8 one sees good agreement near threshold (8-8.5 eV) between the two energy-loss measurements. Away from threshold (10-12 eV) – where the effects of the sharp Wigner onset and the varying electron energy spreads are less important – there is also good agreement between present energy-loss results and the results of Refs. [7,8]. The results of Ref. [9] are lower than either present data or other optical data [7,8] in the 10-12 eV energy range, although the difference is approaching the limits of the combined total error bars [22].

There are additionally three theories available for comparison. These are a Coulomb-Born

(CB) calculation [23], a two-state close-coupling (2CC) calculation [23], and a more recent nine-state R-matrix (9CC) calculation [24]. These three theories are also presented in Fig. 8, with the first two shown at two electron-energy spreads – 0.17 and 2.3 eV – for comparison with the energy-loss and optical-emission data, respectively. Agreement among the theories and the energy-loss experiments at threshold is good. In the 9-12 eV range the 9CC calculation lies towards the lower range of the present energy-loss data; while agreement of the present data with the 2CC and CB in this energy range is good. The agreement of the two optical-emission experiments with the 9CC is somewhat better than with the CB or 2CC. The data of Ref. [9] now lie only about 10-20% below the 9CC theory, but 20-30% below the optical and energy-loss data.

IV. CONCLUSIONS

Present energy-loss measurements of absolute excitation cross sections for the 2s $\rightarrow$ 2p transition in e + C^{3+} collisions are in good agreement with a previous energy-loss measurement at threshold [6]; and above threshold with optical-emission results of Refs. [7,8]. Present results above threshold are about 35% higher than the optical-emission data of Ref. [9]. Agreement of present results with three theories – a Coulomb-Born calculation [23], a two-state close coupling calculation [23], and a nine-state R-matrix calculation [24] – is satisfactory throughout the energy range (8-12 eV) of the present energy-loss measurements.

ACKNOWLEDGMENTS

References

[1]   U. Feldman, W. E. Behring, W. Curdt, U. Schühle, K. Wilhelm, P. Lemaire, and T. M. Moran, Astrophys. J. Suppl. Ser. **113**, 195 (1997).

[2]   E. Landi, M. Landini, and G. Del Zanna, Astron. Astrophys. **324**, 1027 (1997).

[3]   J. D. Slavin, J. M. Shull, and M. C. Begelman, Astrophys. J. **407**, 83 (1993).

[4]   L. Heroux, Proc. Phys. Soc. **83**, 121 (1964).

[5]   R. C. Isler, R. W. Wood, C. C. Klepper, N. H. Brooks, M. E. Fenstermacher, and A. W. Leonard, Phys. Plasmas **4**, 355 (1997).

[6]   M. E. Bannister, Y.-S. Chung, N. Djurić, B. Wallbank, O. Woitke, S. Zhou, G. H. Dunn, and A. C. H. Smith, Phys. Rev. A **57**, 278 (1998).

[7]   P. O. Taylor, D. Gregory, G. H. Dunn, R. A. Phaneuf, and D. H. Crandall, Phys. Rev. Lett. **39**, 1256 (1977).

[8]   D. Gregory, G. H. Dunn, R. A. Phaneuf, and D. H. Crandall, Phys. Rev. A **20**, 410 (1979).

[9]   D. W. Savin, L. D. Gardner, D. B. Reisenfeld, A. R. Young, and J. L. Kohl, Phys. Rev. A **51**, 2162 (1995).

[10]   D. Hitz, G. Melin, M. Pontonnier, and T. K. Nguyen, *11th Int. ECR Ion Source Workshop* (Groningen , 1993).

[11]   G. Melin, F. Bourg, P. Briand, M. Delaunay, G. Gaudart, A. Girard, D. Hitz, J. P. Klein, P. Ludwig, T. K. Nguyen, M. Pontonnier, and Y. Su, Rev. Sci. Instr. **65**, 1051 (1994).

[12]   C. Liao, S. J. Smith, A. Chutjian, and D. Hitz, Physica Scripta **T73**, 382 (1997).

[13]   A. Chutjian, J. B. Greenwood, and S. J. Smith, APS Topical Conf. on Atomic

Processes in Plasmas (in press, 1998).

[14]   C. Liao, S. J. Smith, D. Hitz, A. Chutjian, and S. S. Tayal, Astrophys. J. **484**, 979 (1997).

[15]   M. T. Bernius and A. Chutjian, Rev. Sci. Instr. **60**, 779 (1989); ibid. **61**, 925 (1990).

[16]   E. W. Bell, X. Q. Guo, J. L. Forand, K. Rinn, D. R. Swenson, J. S. Thompson, G. H. Dunn, M. E. Bannister, D. C. Gregory, R. A. Phaneuf, A. C. H. Smith, A. Müller, C. A. Timmer, E. K. Wåhlin, B. D. DePaola, and D. S. Belić, Phys. Rev. A. **49**, 4585 (1994).

[17]   S. J. Smith, A. Chutjian, J. Mitroy, S. S. Tayal, R. J. W. Henry, K-F. Man, R. J. Mawhorter, and I. D. Williams, Phys. Rev. A **48**, 292 (1993).

[18]   D. A. Dahl, SIMION 3D Version 6.0 User's Manual (Idaho Nat. Engin. Lab. Report No. ICEL.-95/0403).

[19]   M. R. McMillan and J. H. Moore, Rev. Sci. Instr. **51**, 944 (1980).

[20]   S. T. Manson, Phys. Rev. **182**, 97 (1969); C. S. Turner and S. T Manson, to be published.

[21]   S. J. Smith, M. Zuo, A. Chutjian, S. S. Tayal, and I. D. Williams, Astrophys. J. **463**, 808 (1996). In regards table I, note that since there are no metastable levels in C^{3+} the error due its population measurement is taken as zero.

[22]   D. W. Savin (private communication, 1998) reports that the data of Ref. [9] could be low by about 6% due to uncollected photons at the multiplier phototube. While this helps the agreement, it still places their data about 20% below the other experiments and theories.

[23]   N. H. Agee, A. L. Marts, J. B. Mann, and W. D. Robb, Los Alamos Scientific

Laboratory Report No. LA-6691-MS, 1977 (unpublished).

[24] V. M. Burke, J. Phys. B **25**, 4917 (1992).

Table 1. Absolute excitation cross sections for the 2s ^{2}S → 2p ^{2}P transition in e + C^{3+}.

Energy (eV)[a]	Cross Section (10^{-16} cm^2)
7.1	-0.33[b]
7.4	-0.65[b]
7.7	0.01[b]
7.9	0.92[b]
8.0	4.04
8.1	6.05
8.2	6.72
8.4	7.76
8.5	7.38
8.9	6.80
9.1	6.83
9.2	6.59
9.6	6.95
9.8	6.21
10.0	6.08
10.1	5.48
10.4	6.49
10.6	5.42
10.7	5.71
11.1	5.40
11.6	5.72
12.1	5.25

[a] The electron energy scale is accurate to ±0.05 eV.

[b] Non-zero values below threshold include effects of the electron energy spread and statistical errors in the experiment.

Figure Captions

Figure 1　Configuration (not to scale) of the JPL MCI facility. (**L1-L7**), three-element focusing lenses, (**B**) differential pumping baffle, (**D**) deflector plates, (**SM**) mass/charge selection magnet, (**MP**) electron merging plates, (**AP**) electron analyzing plates, (**MI**) electron mirror to reflect inelastically-backscattered electrons into the forward PSD, (**EA**) electronic aperture to limit the transmission of elastically-scattered electrons, (**DP**) trochoidal plates to deflect parent electron beam out of the scattering plane, (**G**) retarding grids, (**PSD**) position-sensitive detector, (**CE**) charge-exchange cell, (**MCP**) microchannel plate, and (**PMT**) multiplier phototube. The three beam lines after the beam switcher are for excitation (used here), *f*-value (using a Kingdon trap), and X-ray emission/charge-exchange measurements.

Figure 2　Schematic diagram of the PC-based system control and data acquisition flow lines.

Figure 3　Schematic of the "electronic aperture" used to filter elastically-scattered electrons with the larger Larmor gyroradii. This end-on view shows sixteen rods (dark circles) symmetrically placed about the merged electron and ion beams (shaded central region). Light lines are calculated equipotentials. Equal and opposite potentials are placed on adjacent rods, and unwanted electron are ejected into the rods or the positively-biased shields.
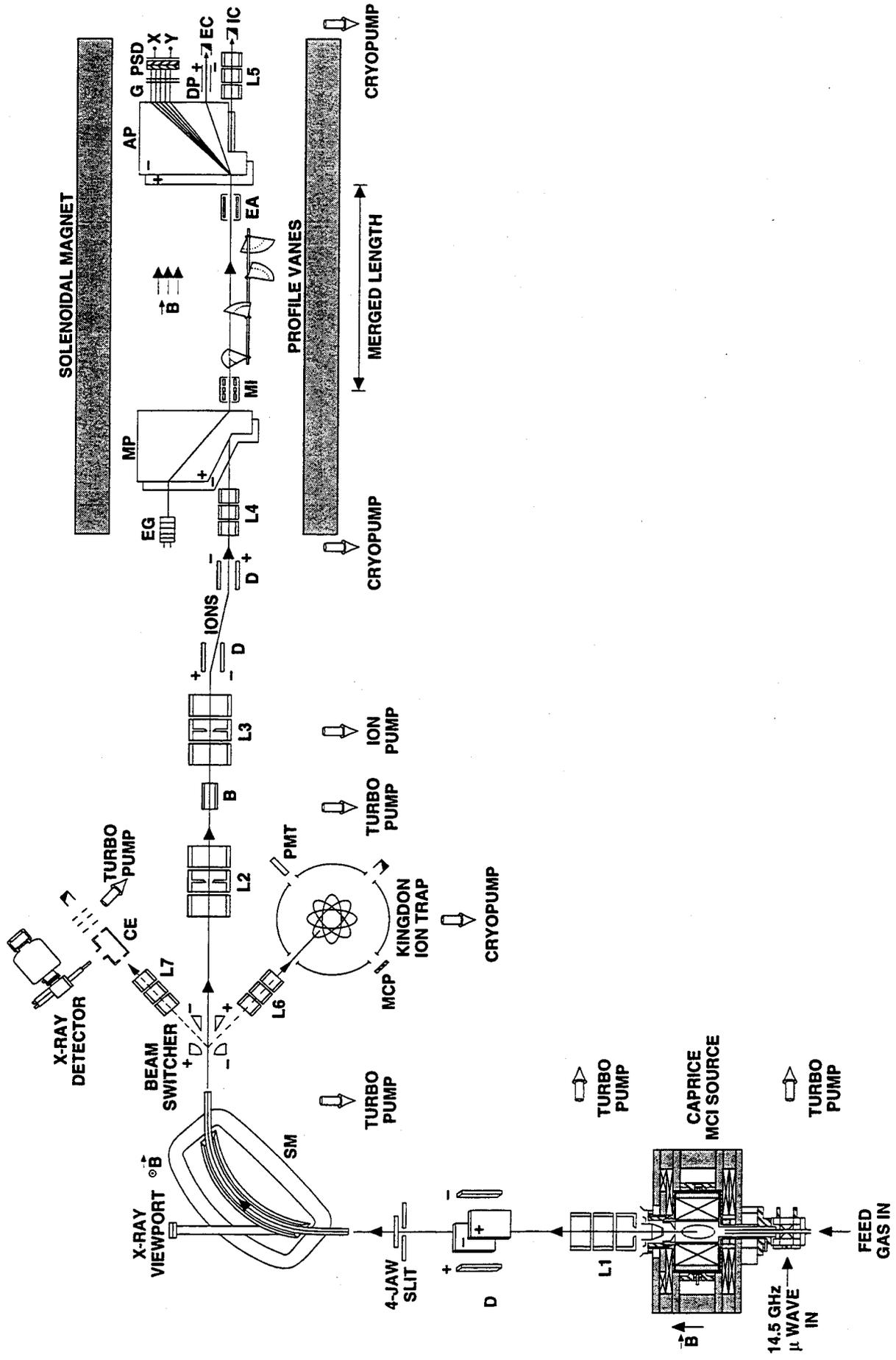
Figure 4　Magnitude of the net electric field of the EA as a function of radial distance from the central axis. Each curve is labeled by the alternate voltages placed on the 16 rods. The center of the rods is at 7.50 mm, with each rod 2.00 mm dia.
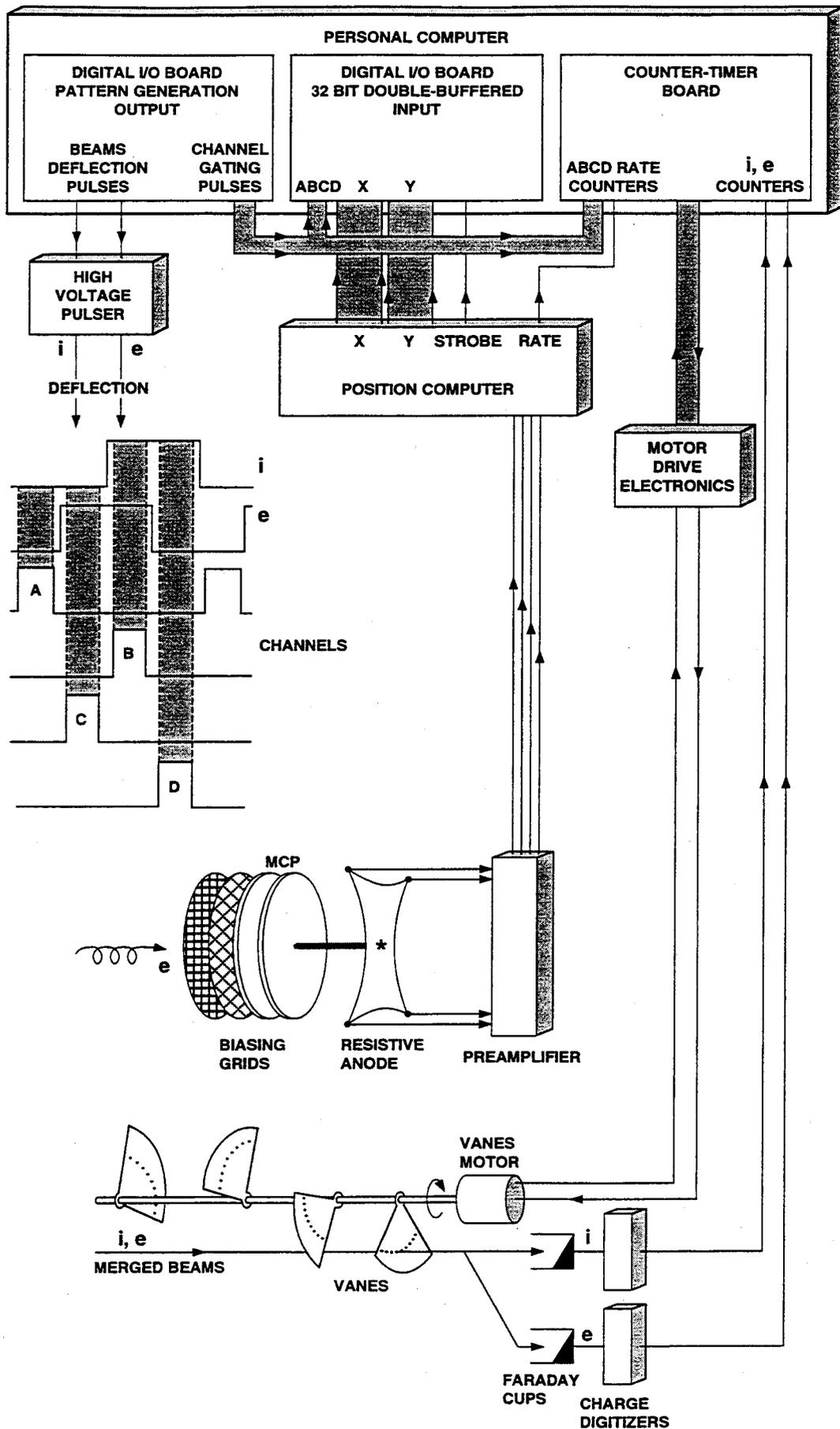
Figure 5   Sample electron trajectories for 60° scattering at the indicated electron energies, with ± 200 V on alternate poles, and as viewed along the multipole or solenoidal B-field axis.
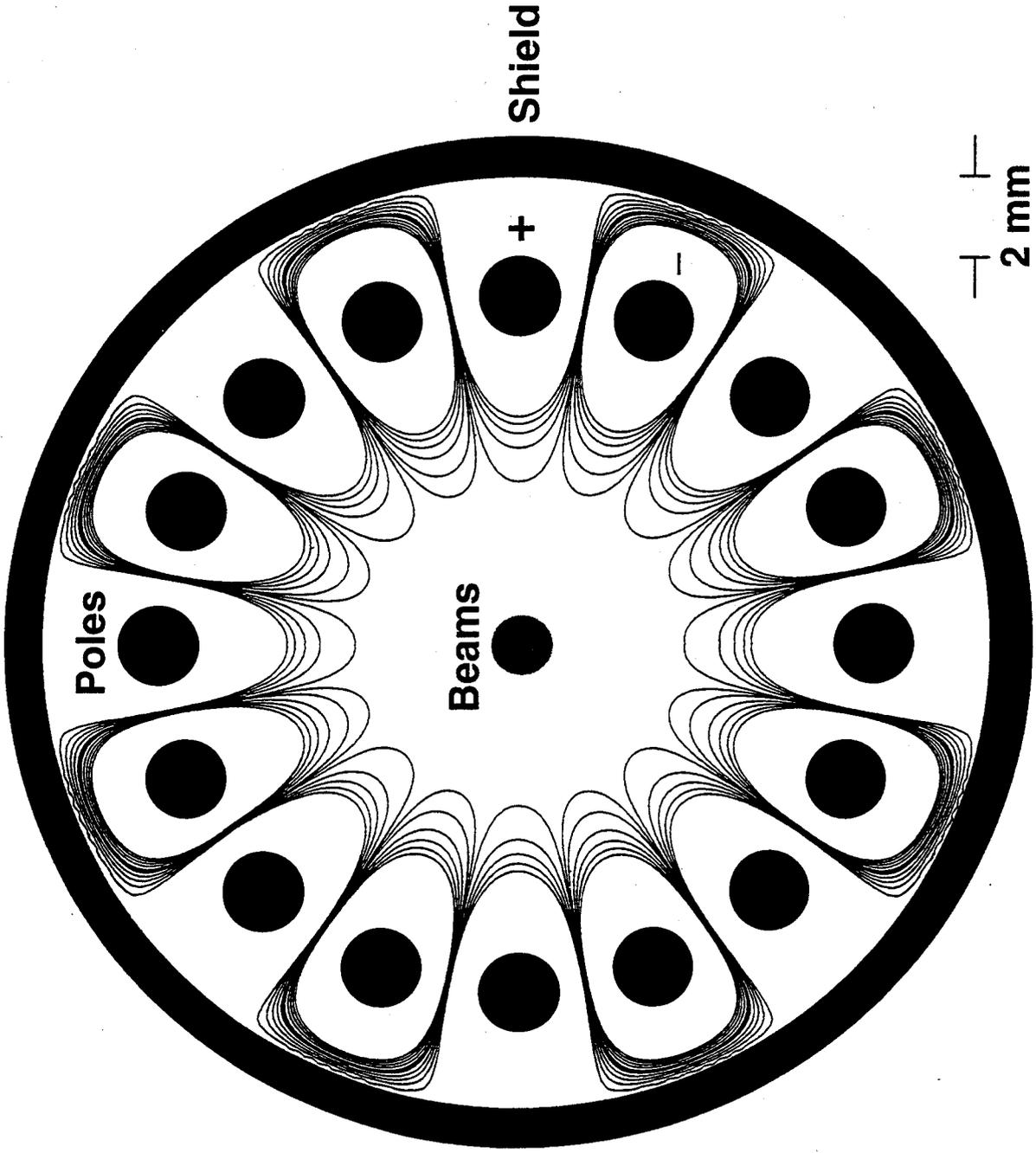

Figure 6   Fraction of electrons transmitted as a function of the maximum excursion of the electron from the center of the EA, at the indicated solenoidal magnetic fields.   The alternating potentials for adjacent rods are indicated on each curve. The 16 poles are centered on a radius of 7.50 mm.
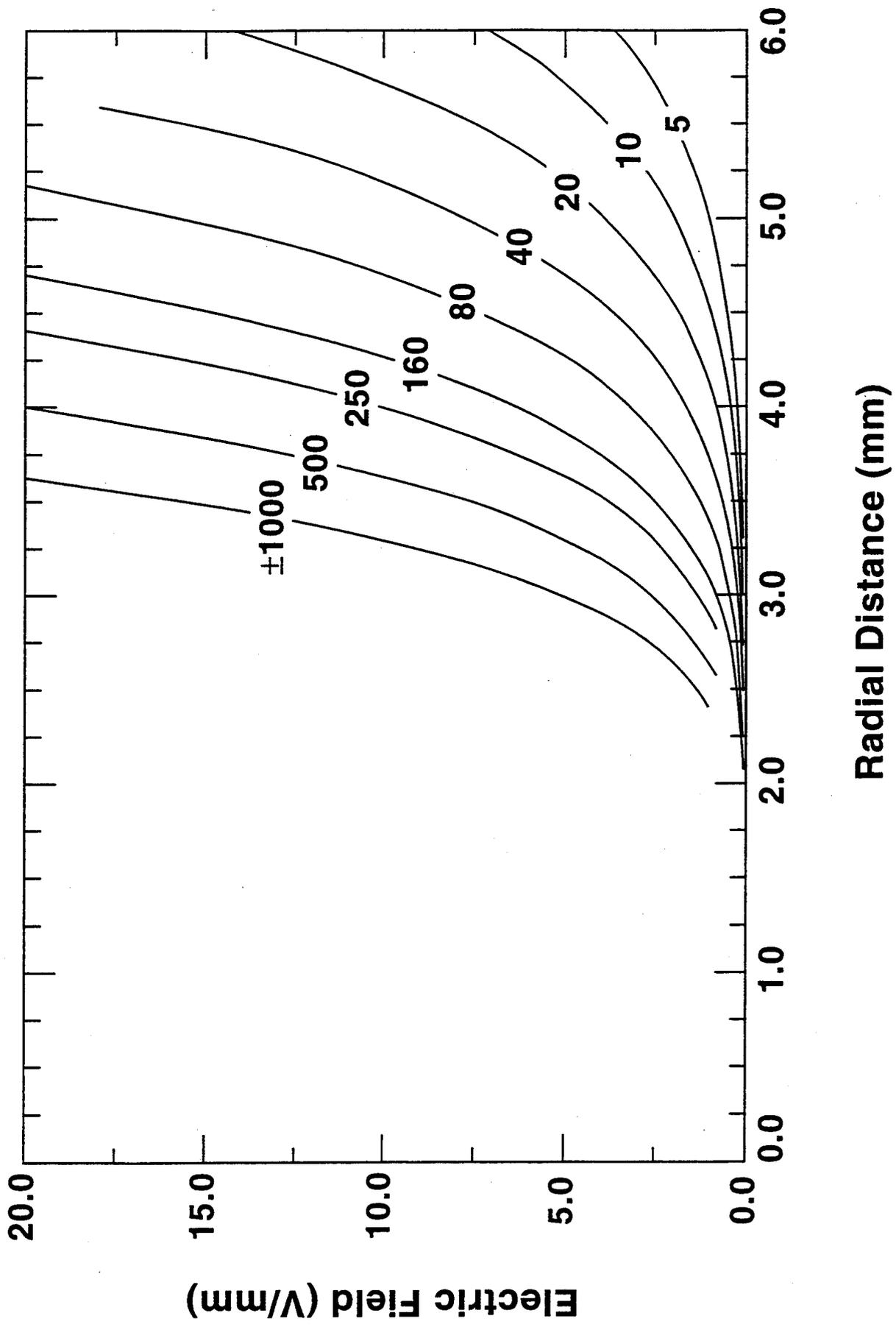

Figure 7   SIMION 3D simulations of the action of the electronic aperture (EA). Shown are 20 trajectories in three cases corresponding to a 9 eV CM energy: (a) elastically-scattered electron signal with the EA "on" (± 300 V on alternate rods); (b) same as (a), but with the EA voltages "off;" (c) 1 eV inelastically-scattered electrons with EA voltages "on," to be compared with (a). See Fig. 1 for other notation.

Figure 8   Experimental cross sections vs CM energy for excitation of the 2s ^{2}S → 2p ^{2}P transition in e + C^{3+} . Present energy-loss results are given as filled circles, with full absolute error bars shown at the 90% confidence level (1.7σ).   Other results are: energy-loss measurements near threshold (open circles with mainly relative error bars [6]), optical-emission measurements (filled square with relative-error bars [9]; open triangles with relative-error bars [7,8]. The solid line is a Coulomb-Born calculation [23] folded with 0.17 eV and 2.3 eV FWHM Gaussian electron-energy distributions of Ref. [6] and Refs. [7,8], respectively. The dashed line is a two-state close coupling calculation [23] convoluted with a 2.3 eV electron-energy distribution and shifted to the spectroscopic threshold for comparison with measurement.   The linked line represents results in the nine-state R-matrix calculation of Ref. [24], as digitized from an expanded Fig. 2 of that paper.
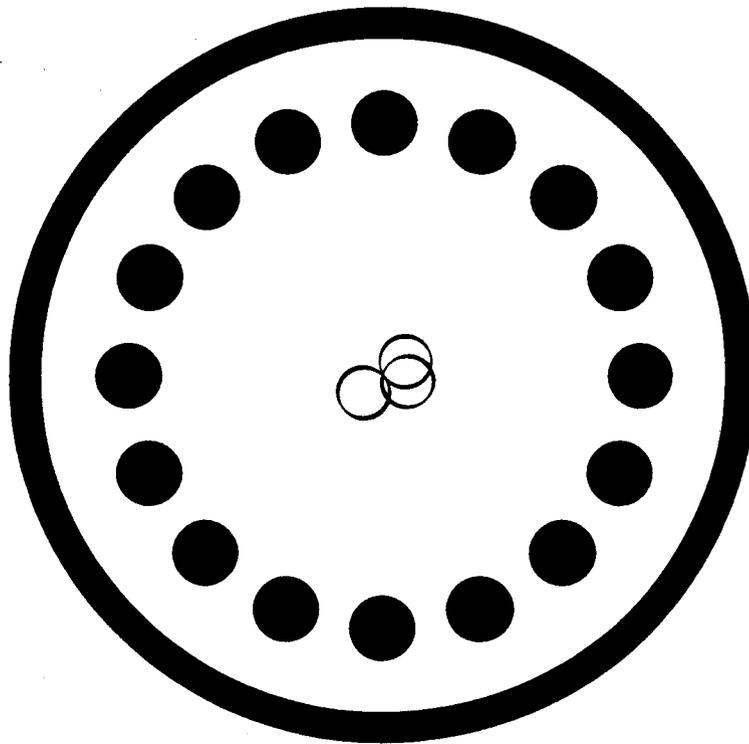
PERSONAL COMPUTER

DIGITAL I/O BOARD
PATTERN GENERATION
OUTPUT

BEAMS
DEFLECTION
PULSES

CHANNEL
GATING
PULSES

DIGITAL I/O BOARD
32 BIT DOUBLE-BUFFERED
INPUT

ABCD   X   Y

COUNTER-TIMER
BOARD

ABCD RATE
COUNTERS

i, e
COUNTERS

HIGH
VOLTAGE
PULSER

i   e

DEFLECTION

X   Y   STROBE   RATE

POSITION COMPUTER

MOTOR
DRIVE
ELECTRONICS

i

e

A

B

CHANNELS

C

D

MCP

e

BIASING
GRIDS

RESISTIVE
ANODE

PREAMPLIFIER

VANES
MOTOR

i, e

MERGED BEAMS

VANES

i

e

FARADAY
CUPS

CHARGE
DIGITIZERS

2

Shield

Poles

Beams

+

−

⊥
2 mm
⊥

3

Electric Field (V/mm) vs Radial Distance (mm)

Contour labels: ±1000, 500, 250, 160, 80, 40, 20, 10, 5

4

1.0 eV

$\otimes$
$\vec{B}$

9.0 eV

$\otimes$
$\vec{B}$

5

6

(a)

9 eV
±300 V

**beams
direction**

EA

AP

PSD

EC

DP

(b)

9 eV
0 V

(c)

1 eV
±300 V

7

8